BMC Oral Health

RESEARCH

Open Access

Identification and validation of autophagy-related genes influenced by paris polyphylla in tongue cancer using network pharmacology

Jing Zhou[1,2,3†], Hongrong Zhang[1,2†], Lingzhi Ma[1,2], Yanyan Chen[2], Zhongshun He[1,2,3] and Biao Xu[1,2*]

Abstract

Background Tongue squamous cell carcinoma (TSCC) represents the most prevalent form of head and neck squamous cell carcinomas, comprising approximately one-third of all oral cancers. Paris polyphylla(PP) exhibit promising anti-tumor properties, yet their underlying mechanisms remain elusive. This study offers novel insights into the molecular mechanisms underlying TSCC treatment with PP and establishes a theoretical basis for their clinical application.

Methods Employing transcriptomics and network pharmacology methodologies, we identified autophagy-related key genes associated with the effects of PP. These genes were subjected to KEGG and GO enrichment analyses to determine their related functions. In vitro, CAL-27 cells were treated with 10, 30, and 60 μg/ml of PP for 24 h to assess tumor cell proliferation, apoptosis, and autophagy-related markers.

Key findings.

Molecular docking of MAPK3 and PSEN1 with PP revealed stable hydrogen bond interactions, indicating the therapeutic potential of these saponins in TSCC through the autophagy pathway. In vitro experiments demonstrated significant inhibition of proliferative activity in tongue squamous carcinoma CAL-27 cells and promotion of tumor cell apoptosis by PP. Western blot analysis confirmed alterations in the expression of autophagy markers P62, LC3B, and Beclin1 following treatment, suggesting activation of the autophagy pathway.

Conclusions Our results suggest that PP inhibits tumor cells through the autophagy pathway, in which MAPK3 and PSEN1 play a role as potential functional molecules.

Keywords TSCC, Paris polyphylla, MAPK3, PSEN1, Apoptosis

Introduction

Tongue squamous cell carcinoma is the most aggressive malignant tumor among head and neck squamous cell carcinomas [1], significantly impairing speech and swallowing functions [2]. The main treatment approach is surgical removal, yet patients often experience a decline in postoperative quality of life, with the five-year survival rate lingering below 60% [3, 4]. Moreover, the active mobility of the tongue and its complex lymphatic and vascular systems contribute significantly to

†Jing Zhou and Hongrong Zhang contributed equally to this work.

*Correspondence:
Biao Xu
xubiao@kmmu.edu.cn
[1] Department of Oral and Maxillofacial Surgery, Affiliated Stomatology Hospital of Kunming Medical University, Kunming 650106, China
[2] Yunnan Key Laboratory of Stomatology, Kunming 650106, China
[3] Department of Stomatology, Yan'an Hospital Affiliated to Kunming Medical University, 245 Renmin East Road, Kunming 650106, China

the invasion and metastasis of cancer cells [5, 6],making it essential to incorporate additional adjunctive treatments. Commonly used therapies include immunotherapy, targeted drug therapy, and laser ablation therapy [7]. Simultaneously, exciting advancements have been made in research on non-coding RNAs and their role in regulating cancer cell resistance [8]. Our previous studies have focused on the potential anti-cancer effects of Paris polyphylla (PP). Unlike traditional therapies, PP offers a multi-targeted treatment mechanism that may produce synergistic effects when combined with other therapies or used alone. Notably, its ability to regulate autophagy is particularly significant in cancer biology, making PP a promising candidate for treating TSCC and warranting further investigation.

In tradional Chinese medicine, Paris polyphylla, or Chonglou, is celebrated for its medicinal benefits [9]. This herb primarily contains saponins but also includes β-ecdysone, polysaccharides, flavone glycosides, and amino acids, which possess anti-inflammatory, analgesic, and anti-tumor properties [10, 11]. Research indicates that extracts of PP can effectively suppress tumor cells while demonstrating low toxicity. These extracts work through various mechanisms such as cytotoxicity, induction of apoptosis in tumor cells, anti-angiogenesis, inhibition of tumor cell proliferation, and immune system modulation [12–14].

Numerous natural medicinal molecules can target the autophagy mediated by the PI3K/AKT/mTOR pathway, effectively inhibiting tumor growth [15]. Autophagy, essential for transporting various cellular products to lysosomes for degradation and recycling, maintains cellular homeostasis under normal conditions by removing dysfunctional organelles and misfolded proteins [16, 17]. However, autophagy plays a complex role in cancer; it can either promote or suppress tumor growth depending on the disease stage and tumor microenvironment. Despite its dual role, the focus on autophagy as a means to inhibit tumor growth remains a significant area of research [16, 18].

This study identified the molecular mechanisms by which PP affects TSCC. Through in vitro experiments and transcriptomic analysis, we aimed to uncover the specific molecular mechanisms by which PP inhibits the TSCC cell line (CAL-27), with a particular focus on its effects on cell proliferation, apoptosis, and autophagy processes. Additionally, we identified and validated the critical roles of two autophagy-related genes (ARGs), MAPK3 and PSEN1, in TSCC. This research provides a theoretical foundation for further exploration of the molecular mechanisms of PP in treating TSCC and for developing new adjunctive therapeutic strategies.

Materials and methods

Data download and cleaning

We downloaded RNA-seq data of tongue cancer tissues and normal tongue tissue samples from the GEO database (https://www.ncbi.nlm.nih.gov/geo/). For our analysis, We utilized the GSE34105 [19] dataset as the training set, which includes samples from 62 tongue squamous cell carcinoma (TSCC) cases and 16 normal tissues, and the GSE13601 [20] dataset as the validation set, containing samples from 31 TSCC cases and 26 normal tissues. The tissue samples were sourced from populations in Europe and North America. Normal tissue samples were obtained from healthy volunteers with no history of oral diseases at the time of sample collection, and these samples were confirmed to be free of any abnormal cells through pathological examination. TSCC case samples were collected from patients diagnosed with tongue squamous cell carcinoma. Additionally, we sourced drug target genes from the HERB database (http://ngdc.cncb.ac.cn/databasecommons/database). We also compiled a list of 531 autophagy-related genes (ARGs) from the Human Autophagy Database (HADb, http://www.autophagy.lu/index.html) and the GO_AUTOPHAGY gene set on the GSEA website (http://software.broadinstitute.org/gsea/index.jsp).

Differential gene screening in Tongue Squamous Cell Carcinoma (TSCC)

We performed a differential gene expression analysis by comparing 16 normal tongue tissue samples with 62 TSCC cases from the training set, using the limma package (version 3.44.3). We selected genes based on an adjusted P-value < 0.05 and |Log2FC| > 0.5. To control for false positive rates due to multiple comparisons, we used an adjusted P-value < 0.05 to ensure that the selected genes were statistically significant. Additionally, we set a threshold of |Log2FC| > 0.5 for differential expression, aiming to identify biologically significant gene changes between normal tongue tissue and TSCC samples for inclusion in subsequent analyses. We visualized the results using volcano plots and heatmaps to display the differentially expressed genes.

Identification of candidate differential target ARGs

Utilizing the HERB database (herb.ac.cn), we conducted a search to identify proteins targeted by PP. Following this, we employed the SwissTargetPrediction database (http://www.swisstargetprediction.ch/) to translate these identified target proteins into their corresponding human genes. This procedure resulted in the identification of genes targeted by PP. Next, we intersected the PP target genes with both the differentially expressed genes (DEGs)

and the autophagy-related genes (ARGs) to pinpoint the differential autophagy-related genes (DARGs)(Supplementtary S2).

DARGs enrichment analysis

Utilizing the R package clusterProfiler (v1.58.0), we conducted enrichment analysis with a focus on the KEGG and GO databases. This aimed to uncover shared functions and pathways within the target gene set. We utilized the statistical method of cumulative hypergeometric distribution to determine the frequency of occurrence of a group of genes at specific functional nodes.

PPI network construction

To deepen our understanding of the interactions among the candidate DARGs, we inputted these genes into the protein–protein interaction retrieval tool, STRING (http://string-db.org), to construct a PPI network. Setting the minimum interaction score to 0.4, we employed Cytoscape software (version 3.8.0) to visually represent the network, aiding in the analysis of the complex interplay and connectivity among these genes.

Machine learning algorithm optimization for DARGs

Lasso is a shrinkage estimation method designed to minimize the residual sum of squares while constraining the sum of the absolute values of the regression coefficients to be less than a constant. This method can generate regression coefficients that are strictly zero, resulting in a more interpretable model. Furthermore, we utilized the Support Vector Machine Recursive Feature Elimination (SVM-RFE) technique, an effective method for feature selection that estimates generalization errors and determines the necessary number of features. Through a combined screening strategy involving both the Lasso model and SVM-RFE technology, we identified the optimal DARGs.

Analysis of DARGs expression levels and diagnostic performance

We analyzed the expression patterns of DARGs in both the training and validation datasets, demonstrating the expression levels of DARGs in both diseased and normal samples. Concurrently, we employed ROC (v 1.0.3) analysis to validate the diagnostic potential of DARGs as biomarkers. We also calculated the area under the curve (AUC) to evaluate the performance of each gene in distinguishing between TSCC and normal samples.

Construction of the Drug-Disease Pathway-Key Target Gene Network.

To deepen our comprehension of the interactions between drugs, diseases, and key target genes, we employed pathways associated with TSCC enriched via KEGG. With the Cytoscape software, we created a network diagram visually illustrating the connections among drugs, disease pathways, and key target genes.

Correlation analysis and prognosis analysis of MAPK3 and PSEN1

We used Pearson's correlation coefficient to calculate the correlation between MAPK3 and PSEN1 across various cancers. Pearson's correlation coefficient is one of the most commonly used methods for measuring correlation, particularly suitable for detecting linear relationships between two variables. Additionally, we observed that the expression data for MAPK3 and PSEN1 in most samples approximated a normal distribution, making Pearson's correlation coefficient an appropriate choice.

Pan-cancer RNA-seq data were obtained from the TCGA database (https://tcga-data.nci.nih.gov/tcga). We downloaded and normalized the relevant data before conducting the correlation analysis between MAPK3 and PSEN1. Furthermore, we downloaded RNA-seq data from 338 OSCC cases and 32 normal tissues from TCGA (Supplementary S3), along with the corresponding clinical information (gender, age, tumor stage, survival status, survival time, etc.) (Supplementary S4). The TCGA-OSCC cohort included 329 OSCC patients with complete survival data. Patients were grouped based on the median expression levels of MAPK3 and PSEN1, with those above the median classified as the high-expression group and those below as the low-expression group. We utilized the "survminer"package in R to generate Kaplan–Meier survival curves to compare the survival outcomes between the high-risk and low-risk groups. The log-rank test was used to assess the significance of survival differences between the two groups.

Immune infiltration assessment

To evaluate immune infiltration levels during disease progression in the training set, we initially utilized the ssGSEA algorithm to compute the infiltration levels of 28 immune cell types per sample. Subsequently, we compared the infiltration levels of these immune cells between TSCC and normal samples, and illustrated the variances via heatmaps and box plots. Moreover, we utilized Spearman correlation analysis to explore the associations between key target genes and differentially infiltrated immune cells. The screening threshold was $|cor| > 0.3$ and a P-value < 0.05.

TF-mRNA regulatory network analysis

To delve into the regulatory mechanisms of key target genes in the disease, we utilized the JASPAR database (https://jaspar.genereg.net/) to predict the transcription factors (TFs) associated with these genes. We then

performed motif enrichment analysis on these TFs to enhance our comprehension of their binding affinities and functional roles. Subsequently, we constructed a TF-mRNA regulatory network.

Molecular docking

To perform molecular docking studies, we initially retrieved the 2D structures of active compounds from PubChem (https://pubchem.ncbi.nlm.nih.gov/) and acquired the 3D structures of key target genes from the PDB online platform (https://www.rcsb.org/). Subsequently, we utilized Chem3D software to convert the 2D structures of the active compounds into 3D structures while minimizing their energy states. Following this, all the obtained 3D structures were imported into Autodock 3 software for the processes of dehydration and hydrogen addition. Following that, we employed the principles of semi-flexible molecular docking to conduct the molecular docking using Autodock Vina and then processed the results using Open Babel. Subsequently, the docking outcomes were visualized utilizing PyMOL software.

Impact of PP on the proliferation and apoptosis of CAL27 cells

We established four experimental groups: a control group, and groups treated with 10, 30, and 60 μg/ml of PP, respectively. CAL27 cells in the logarithmic growth phase were seeded in a 96-well plate at a density of 1×10^4 cells/ml, with 100 μl per well. Following the adherence of cells to the well surfaces, they underwent treatment according to their respective groups for 48 h to evaluate cell proliferation. Each treatment group consisted of five replicate wells. Subsequently, 10 μl of CCK-8 reagent was added to each replicate, and the cells were then incubated for an additional 3 h at 37 °C. After the incubation period, the optical density (OD) at 450 nm was measured using a microplate reader, followed by statistical analysis.

For apoptosis detection, cells were seeded at a density of 1×10^5 cells/ml in a 6-well plate, with 1 ml per well. Following cell adhesion, the cells were treated according to their group assignments for 48 h. After treatment, cells were digested, counted, and adjusted to a concentration of 1×10^6 cells/ml. The cells underwent two washes with precooled PBS and were then centrifuged at 1000 rpm for 5 min. Subsequently, the cells were resuspended in 100 μl of 1×Binding Buffer, and 5 μl of Annexin V-FITC was added. Following this, the mixture was incubated at room temperature in the dark for 15 min. After the incubation period, 5 μl of propidium iodide (PI) was added, and the cells were gently mixed. An additional 400 μl of PBS was added and gently mixed. Finally, flow cytometry was performed to detect apoptotic cells, with each treatment group consisting of three replicate samples.

Detection of autophagy and apoptosis-related protein expression in CAL27 cells by Chonglou Saponins

Western Blot Analysis: CAL27 cells treated with PP were seeded at a density of 1×10^5 cells/ml in 6-well plates, with 1 ml per well. Following adherence to the wells, cells were subjected to different treatment conditions for 48 h. Total protein extraction was conducted, and quantification was performed using the BCA method. The expression levels of LC3B (Abcam, ab192890), p62(Abcam, ab109012), and Beclin 1(Abcam, ab302669) were detected using antibodies diluted at 1:2000, with GAPDH (Abcam, ab9485) utilized as an internal control.

Results

Differential gene analysis reveals key DEG and DARG in tongue cancer

Differential gene analysis conducted on the TSCC group and the normal group from the training dataset GSE34105 revealed 3,027 differentially expressed genes (DEGs) associated with tongue cancer. These findings were visualized in a volcano plot (Fig. 1A), highlighting 1,358 upregulated genes and 1,669 downregulated genes (Supplementtary S1). Noteworthy among the upregulated genes in tumor tissues were *MMP12*, *IL2RA*, *IL24*, and *TNFRSF13B*, while prominent downregulated genes included *CRISP3*, *CYP2C18*, *SH3GL3*, *KRT4*, and *SCGB2A1*. A heatmap depicting the expression patterns of these DEGs across all samples (Fig. 1B) revealed distinct expression profiles in control tissues compared to TSCC, this is closely related to tumor heterogeneity. Further analysis showcased an intersection of 249 potential PP target genes and 531 ARGs with the 3,027 tongue cancer DEGs, delineated in a Venn diagram (Fig. 1C, Supplementtary S2). This intersection highlighted 5 key DARGs: *BCL2L1*, *PSEN1*, *CASP3*, *MAPK8*, and *MAPK3*.

The top 5 significant GO and KEGG enrichment results were depicted in Fig. 1D and E, respectively. GO enrichment analysis revealed that DARGs are implicated in cellular responses to abiotic stimulus, cellular responses to environmental stimulus, macroautophagy, regulation of macroautophagy and response to oxidative stress. Regarding KEGG pathways, the top 5 pathways identified were Apoptosis, Apoptosis-multiple species, Human immunodeficiency virus 1 infection, Pathways of neurodegeneration-multiple diseases and Toxoplasmosis. These findings suggest a pivotal role of DARGs in tumor development, particularly in relation to autophagy and apoptosis. Furthermore, in the context of external pharmacological interventions with PP, DARGs serve as

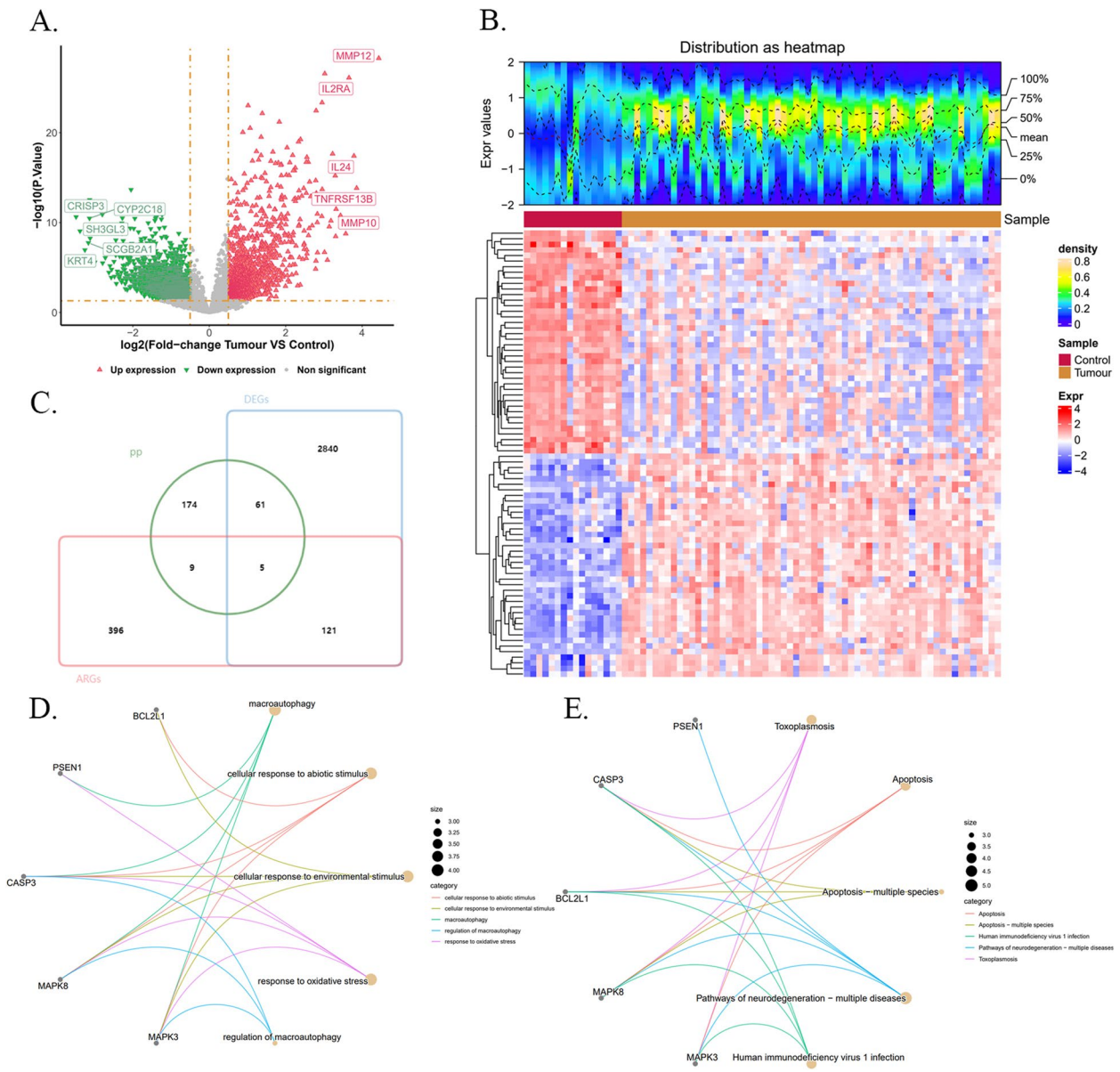

Fig. 1 Selection and Functional Enrichment of DARGs. **A** This is a volcano plot displaying the DEGs between TSCC and normal tissues. the x-axis of the volcano plot represents the fold change in gene expression, while the y-axis represents the corresponding *p*-value. Upregulated genes are denoted by red points, downregulated genes by green points, and genes with no significant difference in expression are depicted in gray. **B** The heatmap shows the expression patterns of DEGs across all samples, with clear differences in expression between normal tissues and TSCC samples. the upper graph illustrates a density distribution diagram showcasing differential gene expression among patients. The lower graph exhibits a heatmap illustrating differential gene expression, with each small square representing the normalized expression level of various genes in each sample; red indicates high expression, whereas blue indicates low expression, with deeper colors indicating stronger expression. **C** This diagram presents the intersection of PP target genes, ARGs, and TSCC differentially expressed genes. PP targets are represented as green circles, DEGs as blue squares, and ARGs as red squares. **D** the results of KEGG enrichment analyses are displayed, with lines connecting significantly enriched pathways and genes; small circles on the left denote genes, while large circles on the right signify pathways. **E** the results of GO enrichment analyses are displayed, with lines connecting significantly enriched pathways and genes; small circles on the left denote genes, while large circles on the right signify pathways

action targets, potentially influencing tumor progression via the autophagy pathway, thereby exerting a significant impact on tumorigenesis.

Feature selection and diagnostic performance assessment for DARGs

We aim to enhance our model's performance through

further training using machine learning techniques, aiming to reduce errors in DARGs and improve generalizability. Initially, we employed SVM analysis to rank each feature by score and iteratively train the model to select the necessary number of features. At the optimal point, with a minimum generalization error of 0.118, we identified five genes: *MAPK3*, *BCL2L1*, *CASP3*, *PSEN1*, and *MAPK8* (Fig. 2A, left). In addition to SVM, we utilized a Lasso regression model, selecting results when the error reached its minimum (lambda.min = 0.0046) (Fig. 2A, middle, right), which identified four DARGs: *MAPK3*, *BCL2L1*, *CASP3*, and *PSEN1*. Further analysis of the expression trends of DARGs in diseases revealed that BCL2L1 ($P < 0.01$) and *PSEN1* ($P < 0.001$) were significantly upregulated in tumors, whereas *CASP3* ($P < 0.001$) and *MAPK3* ($P < 0.0001$) were significantly downregulated in the training set. We further evaluated the diagnostic potential of DARGs, with ROC curve AUC results indicating that all four DARGs possessed AUC values exceeding 0.7, suggesting favorable diagnostic performance (Fig. 2B and C). In the validation set, we similarly examined the differential expression and diagnostic efficacy of these four DARGs. Our analysis revealed that *MAPK3* was downregulated in tumors ($P < 0.05$), while *PSEN1* was upregulated ($P < 0.0001$). Although this finding remained consistent with the validation set, there was no discernible difference in expression levels between *BCL2L1* and *CASP3*, likely attributable to the limited sample size. Additionally, we evaluated the diagnostic potential of *MAPK3* and *PSEN1*, revealing AUC values surpassing 0.7, indicative of robust diagnostic performance (Fig. 2D and E). Recognizing *MAPK3* and *PSEN1* as pivotal genes, we proceeded with further analysis. Expanding our investigation from TSCC to OSCC, we observed differential expression of these key genes in OSCC and confirmed their diagnostic efficacy (Fig. 2F and G).

Correlation between MAPK3 and PSEN1 in *pan-cancer* analysis

Positive correlations were observed between *MAPK3* and *PSEN1* in multiple cancer types, including HNSC, THCA, and PAAD, as shown in Fig. 3A. Furthermore, a positive correlation was evident in the expression of these genes in normal tissues such as the heart, kidney, and colon (Fig. 3B). Specifically, in HNSC, the correlation was visualized with an *R* value of 0.28 and a *p*-value of 8.58e-11, indicating a synergistic effect between *MAPK3* and *PSEN1* in head and neck squamous carcinoma (Fig. 3C). Additional analysis utilizing survival data and RNA-seq from the TCGA-OSCC cohort categorized patients into high and low expression levels, paired with survival status and duration. Our findings reveal that elevated expressions of *MAPK3* ($p = 0.2$) and *PSEN1* ($p = 0.03$) correlate with shorter survival times (Fig. 3D and E). Notably, *PSEN1* emerges as a prognostic marker, with heightened gene expression potentially signifying poorer outcomes. To evaluate the potential synergistic effect of *MAPK3* and *PSEN1*, we conducted a comprehensive analysis considering both genes. Utilizing a multivariate COX regression analysis, we derived a combined risk score model: Risk Score = 0.3**PSEN1*—0.11**MAPK3*. Our results indicate that a higher risk score is associated with a poorer prognosis, underscoring its enhanced predictive capability for outcomes ($P = 0.01$) (Fig. 3F).

Immune score and immunoinfiltration analysis in high and low risk patients. Immune score and tumor microenvironment analysis

Risk Scores were computed for each patient, who were subsequently categorized into high and low-risk groups. Analysis revealed a disparity in immune scores between the high and low-risk groups ($P < 0.01$), with the latter exhibiting higher immune scores (Fig. 4A). Nonetheless, no statistically significant variances were observed in ESTIMATE and Stromal scores ($P > 0.05$). Immune infiltration analysis unveiled that the high-risk group

(See figure on next page.)

Fig. 2 Feature Selection and Diagnostic Performance Assessment for DARGs. **A** the diagram on the left depicts a graph correlating the number of features analyzed with SVM to the generalization error. In the middle diagram, the selection of the regularization parameter λ in Lasso regression and the corresponding error are displayed. The right diagram illustrates the alterations in feature coefficients at various λ values. **B** the box plots illustrate the expression differences between the control group and tumor group in the training dataset GSE34105, with red representing the tumor group and green representing the control group. The x-axis lists the gene names, while the y-axis displays the expression values. **C** ROC curves demonstrate each gene's performance as diagnostic markers in the training dataset GSE34105. A larger area under the curve (AUC) signifies greater method authenticity. **D** box plots illustrate expression differences between the control and tumor groups in the training dataset GSE13601. Red represents the tumor group, and green represents the control group. The x-axis displays gene names, and the y-axis shows expression values. **E** ROC curves depict each gene's performance as diagnostic markers in the training dataset GSE13601. A larger AUC signifies greater method authenticity. **F** box plots display expression differences between the control and tumor groups in the TCGA-OSCC dataset. Red denotes the tumor group, and green denotes the control group. The x-axis lists gene names, and the y-axis shows expression values. **G** ROC curves demonstrate each gene's performance as diagnostic markers in the TCGA-OSCC dataset. A larger area under the curve (AUC) signifies greater method authenticity

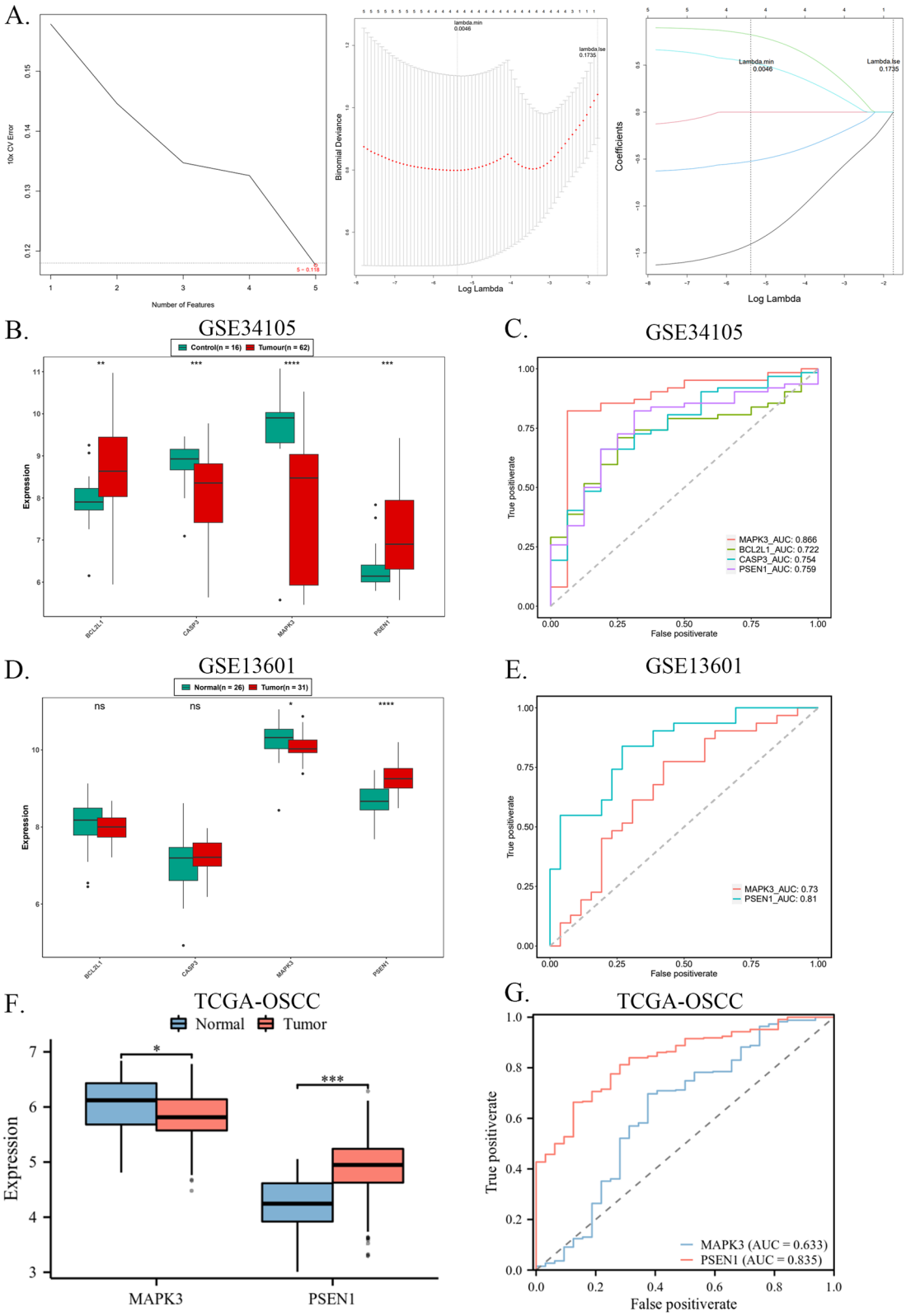

Fig. 2 (See legend on previous page.)

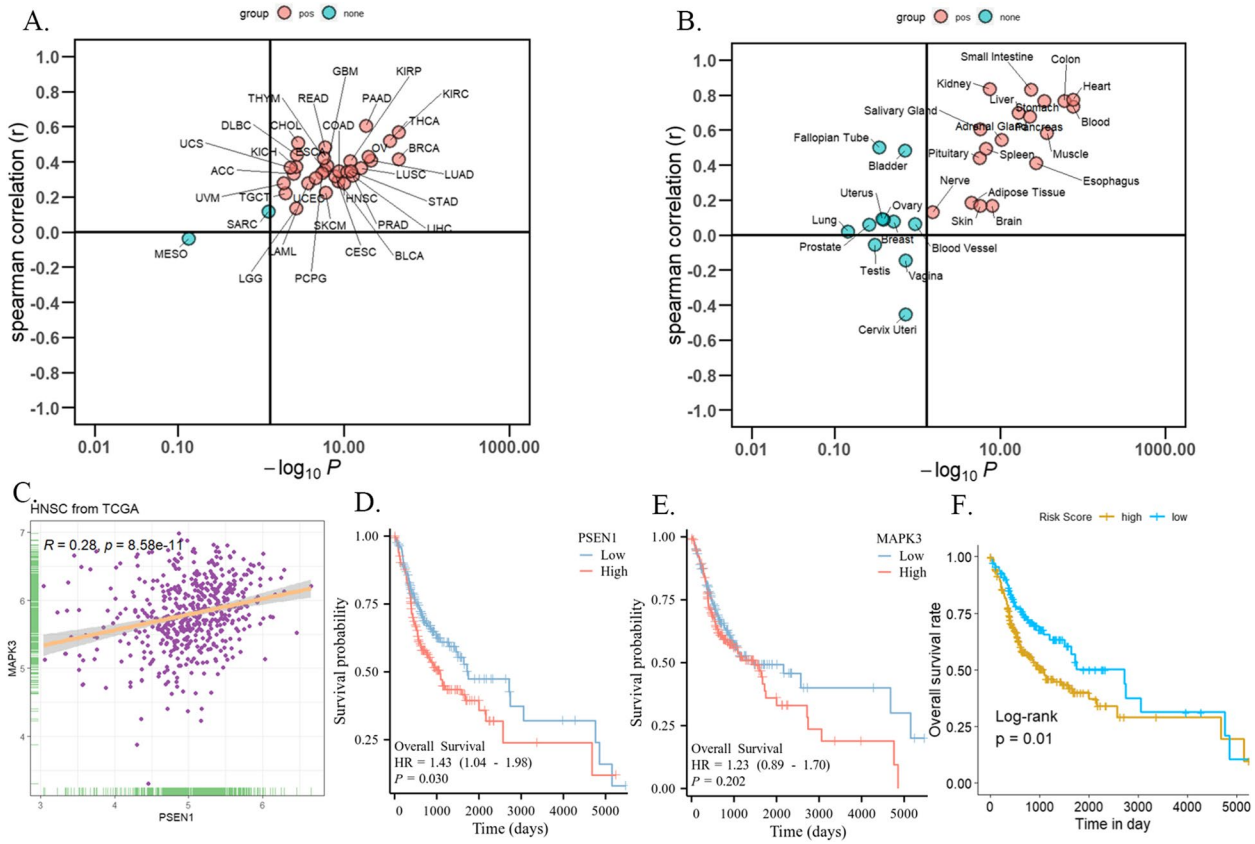

Fig. 3 Examining the correlation between *MAPK3* and *PSEN1* expression and their influence on survival across diverse cancer types. **A** the scatter plot illustrates the Spearman correlation and significance (-log10 *P*-value) between MAPK3 and PSEN1 across various cancer types. Stronger correlations are highlighted in red. **B** the scatter plot demonstrates the correlation and significance of *MAPK3* and *PSEN1* in normal tissues. **C** within head and neck squamous cell carcinoma (HNSC), the scatter plot depicts the correlation between *MAPK3* and *PSEN1*. Individual samples are denoted in purple, and the trend line is represented in orange. **D** Kaplan–Meier curves illustrate the prognostic predictions of *PSEN1*, patients are delineated by blue (low expression) and red (high expression) lines. The vertical axis denotes survival probability, while the horizontal axis indicates survival time. **E** Kaplan–Meier curves illustrate the prognostic predictions of *MAPK3*, patients are delineated by blue (low expression) and red (high expression) lines. The vertical axis denotes survival probability, while the horizontal axis indicates survival time. **F** Kaplan–Meier curves illustrate the prognostic predictions of a risk scoring model, patients are delineated by blue (low expression) and yellow (high expression) lines. The vertical axis denotes survival probability, while the horizontal axis indicates survival time

exhibited diminished levels of activated B cells, activated CD8 T cells, effector memory CD8 T cells, and monocytes, while showcasing elevated levels of CD56bright natural killer cells and memory B cells (Fig. 4B).

Joint role of MAPK3 and PSEN1 in TSCC

Initially, we predicted 78 transcription factors for MAPK3 and 79 for PSEN1 (Fig. 5A). Motif enrichment analysis facilitated the establishment of a TF-mRNA regulatory network. We identified 16 common transcription factors (MYC, FOXP2, ATF2, RELA, ZNF575, TCF3, STAT3, OLIG2, TBX5, MXL1, CREM, EGR1, ZNF384, USF2, SETDB1, and BHLHE40) that collectively regulate the expression and function of both MAPK3 and PSEN1. Further exploration of interactions between drugs, diseases, and key target genes unveiled a network diagram depicting drug-disease-pathway-key target gene relationships. This diagram illustrates the common KEGG pathways shared by *MAPK3* and *PSEN1* with pp (Fig. 5B). These pathways encompass Nucleotide Excision Repair, Fructose and Mannose Metabolism, Mismatch Repair, Oxidative Phosphorylation, Parkinson's Disease, Neuroactive Ligand-Receptor Interaction, DNA Replication, Olfactory Transduction, Proteasome, and Alzheimer's Disease.

Discussion on PP activity and possible docking forms with key genes

We discussed the potential docking configurations of PP activity with key genes and observed that MAPK3

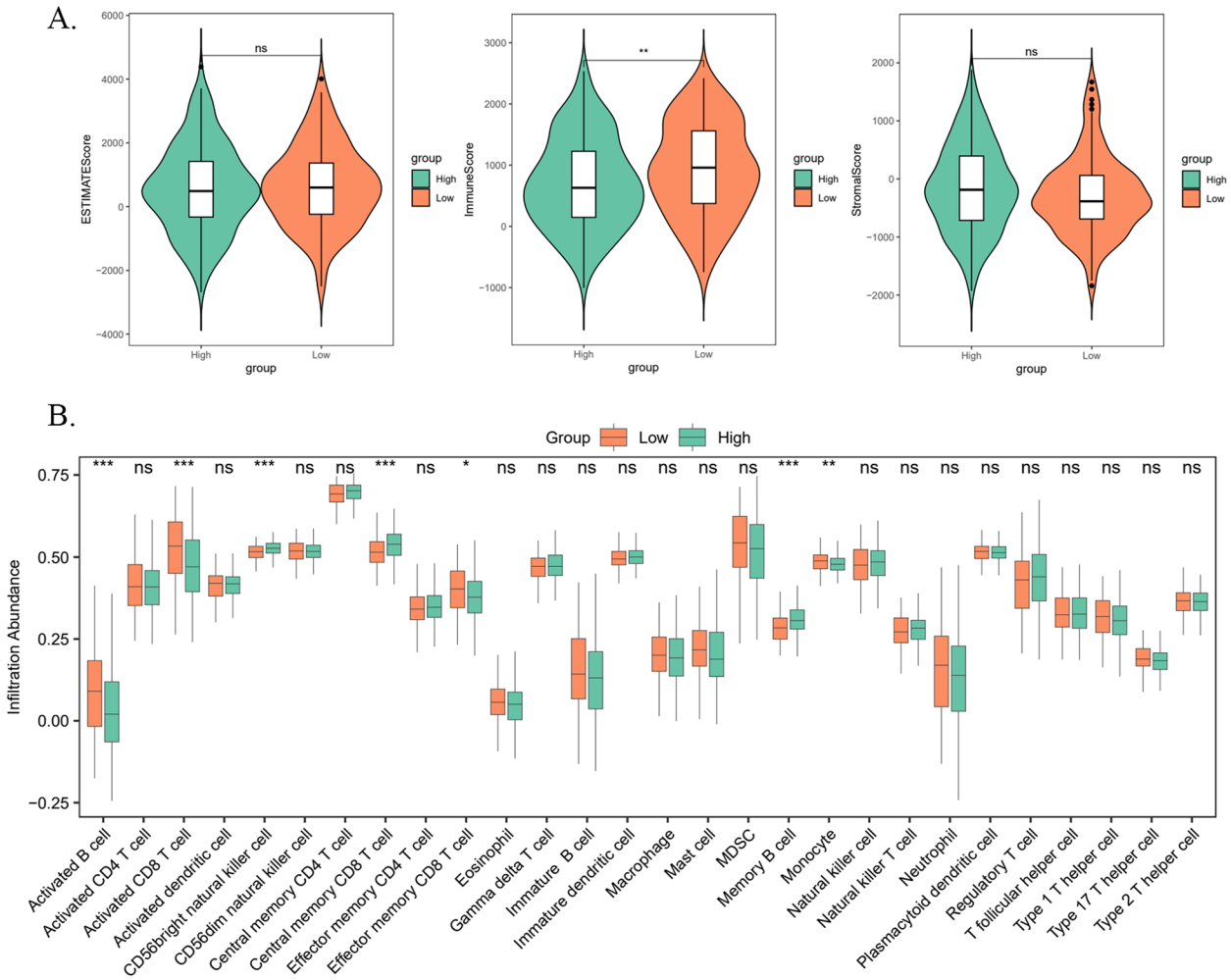

Fig. 4 **A** the analysis comparing immune scores and tumor microenvironment between high and low-risk patient groups included the ESTIMATE scores, immune scores, and stromal scores of patients in each group. Violin plots were employed to depict score distributions in each group, with the y-axis indicating the scores and the x-axis representing the groups. The central white box displays the median and quartiles. **B** box plots illustrated the relative abundance of diverse immune cell types in high-risk and low-risk patient groups, with each cell type listed on the x-axis.The plots denote various levels of statistical significance: "ns" for $P > 0.05$; "*" *for* $P < 0.05$; "**" *for* $P < 0.01$; "***" for $P < 0.001$; "****" for $P < 0.0001$. High-risk groups are represented in orange, while low-risk groups are depicted in green

undergoes molecular docking with the small molecule (Fig. 5C). The recorded molecular binding energy was -9.13, characterized by two hydrogen bonds formed with TYR-219 and TRP-226. Furthermore, *PSEN1* was docked with the small molecule (Fig. 5D), resulting in a binding energy of -7.65 and the formation of a single hydrogen bond with CLR-303. Hydrogen bonds, a type of non-covalent bond, typically facilitate relatively stable interactions in biomolecules. This suggests a stable interaction between the drug molecules and the gene proteins, facilitated by the formation of hydrogen bonds.

PP induces autophagy pathways in CAL27 cells, thereby promoting apoptosis while concurrently inhibiting tumor cell activity

PP induces autophagy pathways in CAL27 cells, promoting apoptosis while simultaneously inhibiting tumor cell activity. Compared to the control group, PP significantly suppressed the proliferation of CAL-27 tongue squamous cell carcinoma cells in a dose-dependent manner, with the most significant inhibition observed at 60 μg/ml, resulting in a survival rate of only 77.4% (Fig. 6A, B). Additionally, we assessed the apoptosis rate of CAL-27 cells upon PP intervention. The control group exhibited

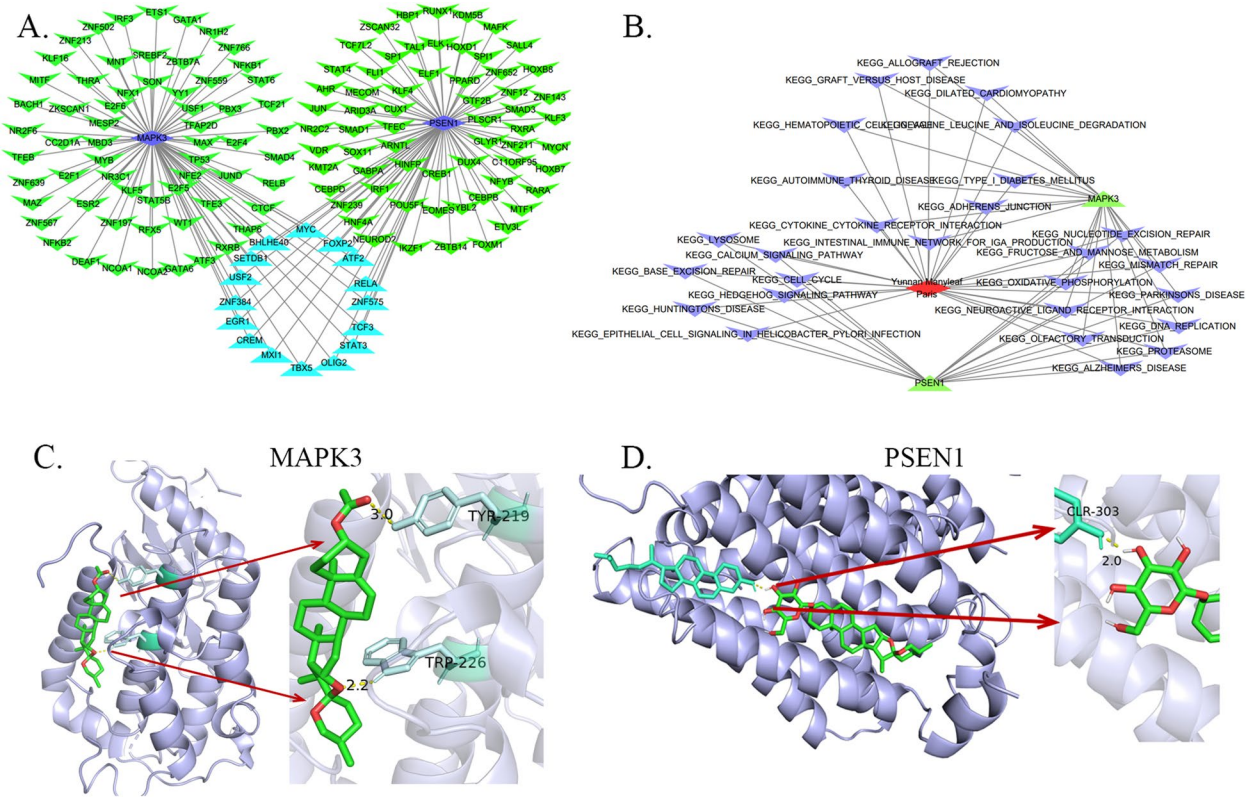

Fig. 5 The presentation encompasses transcription factor networks, disease pathway analysis, and molecular docking studies. **A** The network interaction diagram visually depicts the regulatory network of transcription factors, with emphasis on the *MAPK3* and *PSEN1* genes, highlighted in blue. The green and teal blocks represent transcription factors associated with *MAPK3* and *PSEN1*, respectively. Additionally, the teal blocks denote transcription factors jointly regulating both *MAPK3* and *PSEN1*. **B** the drug-disease-gene network diagram delineates the associations of *MAPK3* and *PSEN1* with various diseases and drug pathways. Each pathway is differentiated by distinct colors, with specific pathways pertinent to the two genes delineated. **C** the 3D structural diagrams elucidate the molecular docking models of *MAPK3* with the small molecule PP, showcasing key interaction sites and hydrogen bonds. The PP small molecule is depicted in green. **D** the 3D structural diagrams elucidate the molecular docking models of*PSEN1* with the small molecule PP, showcasing key interaction sites and hydrogen bonds. The PP small molecule is depicted in green

an apoptosis rate of 9.6%. However, the addition of 10 μg of PP stimulated apoptosis in CAL-27 cells, with apoptotic activity increasing further with higher PP concentrations. Notably, apoptosis rates significantly increased at PP concentrations of 30 and 60 μg (Fig. 6C, D).

Furthermore, we investigated the expression of autophagy-related proteins P62, LC3B, and Beclin1 during PP intervention (Fig. 6E). P62, an autophagy substrate, accumulates when autophagy activity is low and degrades when activity is high. Following PP treatment, P62 levels

(See figure on next page.)

Fig. 6 Effects of PP on Proliferation, Apoptosis, and Autophagy-Related Protein Expression in CAL-27 Cells. **A** CCK-8 Assay: The OD values at 450 nm indicating the proliferation rate of CAL-27 cells after treatment with various concentrations of PP (0, 10, 30, and 60 μg/ml) for 24 h. The data show a dose-dependent inhibition of cell proliferation. **B** Relative Proliferation Rate: Bar graph displaying the relative proliferation rate of CAL-27 cells treated with PP at different concentrations compared to the control group (0 μg/ml). Data are presented as mean ± SD ($n = 3$). *$P < 0.05$, **$P < 0.01$, ****$P < 0.0001$ compared to the control group. **C** Flow Cytometry Analysis of Apoptosis: Flow cytometry scatter plots showing the percentage of apoptotic CAL-27 cells treated with 0, 10, 30, and 60 μg/ml PP. The lower left quadrant (Q1-LL) represents viable cells, the lower right quadrant (Q1-LR) represents early apoptotic cells, the upper right quadrant (Q1-UR) represents late apoptotic cells, and the upper left quadrant (Q1-UL) represents necrotic cells. **D** Apoptosis Rate: Bar graph depicting the apoptosis rate of CAL-27 cells after PP treatment. The percentage of apoptotic cells increased significantly in a dose-dependent manner. Data are presented as mean ± SD ($n = 3$). ns: not significant, *$P < 0.05$, **$P < 0.01$ compared to the control group. **E** Western Blot Analysis of Autophagy-Related Proteins: Western blot images and corresponding bar graphs showing the expression levels of P62, LC3B (LC3BI and LC3BII), and Beclin1 proteins in CAL-27 cells treated with 0, 10, 30, and 60 μg/ml PP. GAPDH was used as a loading control. The bar graphs represent the relative expression levels of these proteins, normalized to GAPDH, indicating an increase in autophagy activity with higher concentrations of PP

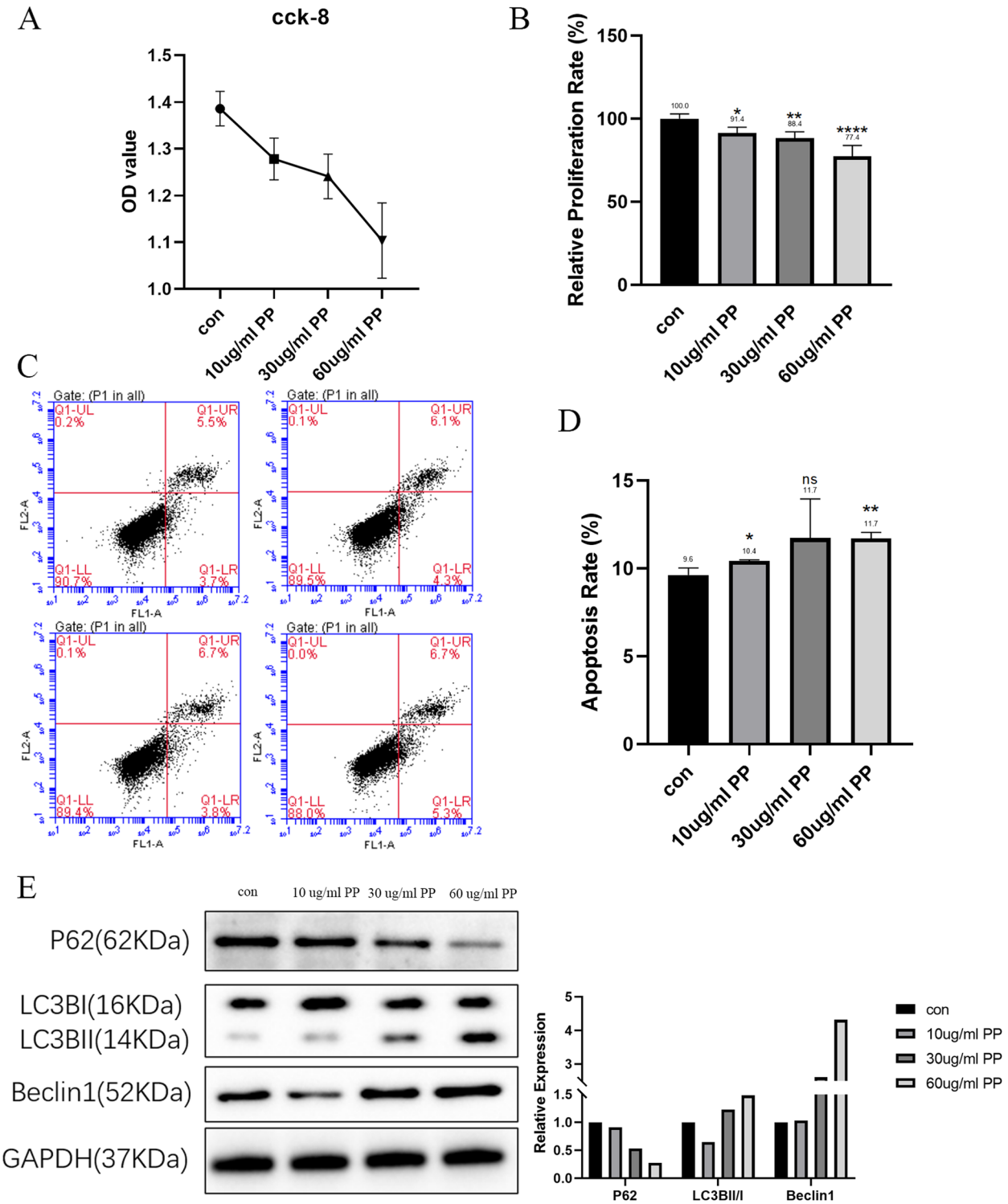

Fig. 6 (See legend on previous page.)

exhibited a negative dose-dependent trend, continually decreasing. Regarding LC3B, its lipidated form (LC3B-II) binds to autophagosome membranes, serving as a marker of autophagy activity. Our data indicate that the LC3BII/I ratio increased compared to the control group under PP intervention, particularly at 30 μg/ml and 60 μg/ml,

strongly suggesting enhanced autophagy activity. Additionally, Beclin1, a crucial protein in autophagy regulation and autophagosome formation, showed increased expression following PP treatment, with significant increases observed at 30 μg/ml and 60 μg/ml, indicating heightened autophagy activity in CAL-27 cells.

Therefore, our findings demonstrate that PP can activate the autophagy pathway in tongue squamous cell carcinoma cells in vitro, simultaneously inhibiting tumor activity and inducing apoptosis. These results may provide a theoretical foundation for using PP in the treatment of tongue squamous cell carcinoma.

Discussion

Autophagy, a conserved cellular degradation system, represents a form of programmed cell death essential for maintaining cellular homeostasis [21]. Research extensively highlights its dual role within cells: under normal conditions, autophagy eliminates damaged or obsolete organelles, proteins, and other cellular structures, thereby stabilizing the internal cellular environment. Moreover, in the face of external stresses such as oxidative stress, nutrient limitation, or infections, autophagy aids cells by providing vital nutrients and energy, thus safeguarding them from damage [22, 23]. Nevertheless, prolonged autophagy activation can trigger cell death. In the context of cancer, this phenomenon manifests bidirectionally. On one hand, autophagy can induce tumor cell death; conversely, tumors might exploit autophagy to reshape the tumor microenvironment, fostering a more favorable milieu for tumor growth [24]. Notably, PP, a widely utilized anticancer medication, demonstrates efficacy in treating various cancers, including gastric cancer [25], non-small cell lung cancer [26], liver cancer [27], and breast cancer [28]. Research has found that inhibiting autophagy can promote the proliferation, migration, and invasion of TSCC cells, while activation of autophagy effectively reduces cancer cell activity [29–31]. Immunohistochemical analysis revealed that Beclin1 and LC3 are downregulated in clinical TSCC samples and are associated with T stage, tumor differentiation, and poor prognosis [17, 29].

A similar approach has been used to study the effects of bioactive compounds on cells, such as the investigation of aflatoxin B1's impact on human hematopoietic stem cells [32]. This parallels our method of studying the effects of PP on TSCC cells, although research on PP's impact on oral tumors is still lacking. Nevertheless, our in vitro experiments have revealed that PP possesses the capability to inhibit the activity of CAL-27 tumor cells. Following PP intervention, we observed activation of the autophagy pathway and upregulation of the apoptosis pathway within these cells. Based on these findings, we propose that in TSCC, PP may activate specific drug targets, thereby regulating autophagy levels within the tumor and ultimately achieving tumor suppression. Nonetheless, the precise targets of PP remain elusive. Through the utilization of network pharmacology, we have identified two potential PP targets, MAPK3 and PSEN1, which have not been previously reported.

MAPK3, or extracellular signal-regulated kinase ERK3, plays a crucial role in the MAPK signaling pathway, influencing cellular processes like proliferation, differentiation, apoptosis, and cancer cell invasion [33]. Activation of MAPK1/3 triggers the ubiquitination and degradation of ULK1. Depletion of ULK1 diminishes mitochondrial autophagy, promoting bone metastasis in breast cancer. However, the upregulation of ULK1, facilitated by the MAP2K/MEK inhibitor trametinib, can restore mitochondrial autophagy and consequently reduce bone metastasis [34]. In biliary tract cancer, MAPK3 can serve as a therapeutic target and has shown promising response rates and survival data [35]. Presenilin-1(PSEN1) plays a crucial role in early-onset Alzheimer's disease (EOAD) and is extensively involved in Notch signaling, β-catenin processing, and calcium metabolism. Studies have reported *PSEN1* overexpression in the autophagy pathway of advanced cervical cancer [36]. In esophageal cancer, miR-193a-3p and PSEN1 may be potential biomarkers for chemoradiotherapy-resistant cancers. miR-193a-3p enhances resistance to radiotherapy and chemotherapy in esophageal cancer by downregulating PSEN1 [37]. *MAPK3* and *PSEN1* show a significant positive correlation across various tumors and tissues. Additionally, they demonstrate distinct expression patterns between tumor and normal tissues, serving as prognostic indicators for patients. As pivotal components of autophagy, *MAPK3* and *PSEN1* can interact with key active molecules of PP, potentially regulating its function.

Currently, there is limited research on *MAPK3* and *PSEN1* in TSCC, but their strong expression correlation at the biological level suggests a promising potential interaction. In the future, we will further investigate the specific mechanisms by which *MAPK3* and *PSEN1* serve as key targets in the regulation of autophagy by PP in TSCC, aiming to provide new strategies for the treatment of TSCC.

Conclusion

Our results suggest that PP inhibits tumor cells through the autophagy pathway, in which MAPK3 and PSEN1 play a role as potential functional molecules.

Abbreviations

TSCC	Tongue squamous cell carcinoma
PP	Paris polyphylla
ARGs	Autophagy-related genes
SVM-RFE	Support Vector Machine Recursive Feature Elimination
TFs	Transcription factors
HNSC	Head and neck squamous cell carcinoma
EOAD	Early-onset Alzheimer's disease

Supplementary Information

The online version contains supplementary material available at https://doi.org/10.1186/s12903-024-04784-8.

Supplementary Material 1.

Acknowledgements
Thank you to Kunming Medical University for your help in this project

Authors' contributions
Manuscript writing, conducted literature searches, and participated in data cleaning, processing, and data visualization, J and H; contributed to data processing and assisted in interpreting the results of data analysis L, Y and Z; provided major contributions, including project design, determination of research direction, supervised data analysis, and oversaw the entire research process, B.X.

Funding
These studies were supported by Basic Research Project of Science and Technology Department of Yunnan Province (202301AY070001-288) and Training of Technological Innovation Talents in Yunnan Province (202405AD350091).

Availability of data and materials
Detailed data are available from the corresponding author upon reasonable request.

Declarations

Ethics approval and consent to participate
Not applicable.

Consent for publication
Not applicable.

Competing interests
The authors declare no competing interests.

Received: 15 July 2024 Accepted: 20 August 2024
Published online: 30 August 2024

References

1. Karatas OF, et al. MicroRNAs in human tongue squamous cell carcinoma: From pathogenesis to therapeutic implications. Oral Oncol. 2017;67:124–30.
2. Aldelaimi AAK, et al. Tumors of Craniofacial Region in Iraq (Clinicopathological Study). J Res Med Dent Sci. 2021;9(1):66–71.
3. Peng Y, et al. Single-cell profiling of tumor-infiltrating TCF1/TCF7(+) T cells reveals a T lymphocyte subset associated with tertiary lymphoid structures/organs and a superior prognosis in oral cancer. Oral Oncol. 2021;119: 105348.
4. Sarode G, et al. Epidemiologic aspects of oral cancer. Dis Mon. 2020;66(12): 100988.
5. Yang X, et al. Prognostic impact of perineural invasion in early stage oral tongue squamous cell carcinoma: Results from a prospective randomized trial. Surg Oncol. 2018;27(2):123–8.
6. Muller S, Tilakaratne WM. Update from the 5th Edition of the World Health Organization Classification of Head and Neck Tumors: Tumours of the Oral Cavity and Mobile Tongue. Head Neck Pathol. 2022;16(1):54–62.
7. Khalil AA, et al. Advances in Diagnosis and Treatment of Basal Cell Carcinoma. J Craniofac Surg. 2024;35(2):e204–8. https://doi.org/10.1097/SCS.0000000000009959. Epub ahead of print.
8. Saleh RO, et al. lncRNA-microRNA axis in cancer drug resistance: particular focus on signaling pathways. Med Oncol. 2024;41(2):52.
9. Zhou N, et al. Genetic Diversity, Chemical Components, and Property of Biomass Paris polyphylla var. yunnanensis. Front Bioeng Biotechnol. 2021;9:713860.
10. Li J, et al. Therapeutic effects on cancer of the active ingredients in rhizoma paridis. Front Pharmacol. 2023;14:1095786.
11. Ahmad B, et al. Molecular mechanisms of anticancer activities of polyphyllin VII. Chem Biol Drug Des. 2021;97(4):914–29.
12. Yu Q, et al. Polyphyllin D induces apoptosis in U87 human glioma cells through the c-Jun NH2-terminal kinase pathway. J Med Food. 2014;17(9):1036–42.
13. Watanabe S, et al. Polyphyllin D induces necroptosis in neuroblastoma cells (IMR-32 and LA-N-2) in mice. Pediatr Surg Int. 2023;39(1):196.
14. Dong RF, et al. Discovery of a potent inhibitor of chaperone-mediated autophagy that targets the HSC70-LAMP2A interaction in non-small cell lung cancer cells. Br J Pharmacol. 2023:1–23. https://doi.org/10.1111/bph.16165. Epub ahead of print.
15. Xu Z, et al. Targeting PI3K/AKT/mTOR-mediated autophagy for tumor therapy. Appl Microbiol Biotechnol. 2020;104(2):575–87.
16. Debnath J, Gammoh N, Ryan KM. Autophagy and autophagy-related pathways in cancer. Nat Rev Mol Cell Biol. 2023;24(8):560–75.
17. Ren Y, et al. An autophagy-related long non-coding RNA signature in tongue squamous cell carcinoma. BMC Oral Health. 2023;23(1):120.
18. Singh SS, et al. Dual role of autophagy in hallmarks of cancer. Oncogene. 2018;37(9):1142–58.
19. Rentoft M, et al. Transcriptional profiling of formalin fixed paraffin embedded tissue: pitfalls and recommendations for identifying biologically relevant changes. PLoS ONE. 2012;7(4):e35276.
20. Estilo CL, et al. Oral tongue cancer gene expression profiling: Identification of novel potential prognosticators by oligonucleotide microarray analysis. BMC Cancer. 2009;9:11.
21. Wang H, et al. Autophagy in Disease Onset and Progression. Aging Dis. 2024;15(4):1646–71.
22. Cui D, Xiong X, Zhao Y. Cullin-RING ligases in regulation of autophagy. Cell Div. 2016;11:8.
23. Liu J, et al. Autophagy, a double-edged sword in anti-angiogenesis therapy. Med Oncol. 2016;33(1):10.
24. Sorice M. Crosstalk of Autophagy and Apoptosis. Cells. 2022;11(9):1479.
25. Hu C, et al. Polyphyllin B Suppresses Gastric Tumor Growth by Modulating Iron Metabolism and Inducing Ferroptosis. Int J Biol Sci. 2023;19(4):1063–79.
26. Teng JF, et al. Polyphyllin VI Induces Caspase-1-Mediated Pyroptosis via the Induction of ROS/NF-κB/NLRP3/GSDMD Signal Axis in Non-Small Cell Lung Cancer. Cancers (Basel). 2020;12(1):193.
27. Yang R, et al. Polyphyllin I induced ferroptosis to suppress the progression of hepatocellular carcinoma through activation of the mitochondrial dysfunction via Nrf2/HO-1/GPX4 axis. Phytomedicine. 2024;122: 155135.
28. Yang Q, et al. Polyphyllin VII protects from breast cancer-induced osteolysis by suppressing osteoclastogenesis via c-Fos/NFATc1 signaling. Int Immunopharmacol. 2023;120: 110316.
29. Wang Y, et al. Decrease of autophagy activity promotes malignant progression of tongue squamous cell carcinoma. J Oral Pathol Med. 2013;42(7):557–64.
30. Shi F, et al. Glaucocalyxin A induces apoptosis and autophagy in tongue squamous cell carcinoma cells by regulating ROS. Cancer Chemother Pharmacol. 2021;88(2):235–46.
31. Chen K, et al. ARNTL inhibits the malignant behaviors of oral cancer by regulating autophagy in an AKT/mTOR pathway-dependent manner. Cancer Sci. 2023;114(10):3914–23.
32. Al-Ouqaili M, Musleh M, Al-Kubaisi S. Depending on HPLC and PCR, detection of aflatoxin B1 extracted from Aspergillus flavus strains and it's cytotoxic effect on AFB treated-hematopoietic stem cells obtained from human umbilical cord. Asian Journal of Pharmaceutics. 2018;12:1048.

33. Lu N, Malemud CJ. Extracellular Signal-Regulated Kinase: A Regulator of Cell Growth, Inflammation, Chondrocyte and Bone Cell Receptor-Mediated Gene Expression. Int J Mol Sci. 2019;20(15):3792.
34. Deng R, et al. MAPK1/3 kinase-dependent ULK1 degradation attenuates mitophagy and promotes breast cancer bone metastasis. Autophagy. 2021;17(10):3011–29.
35. Kam AE, Masood A, Shroff RT. Current and emerging therapies for advanced biliary tract cancers. Lancet Gastroenterol Hepatol. 2021;6(11):956–69.
36. Campos-Parra AD, et al. Comprehensive transcriptome analysis identifies pathways with therapeutic potential in locally advanced cervical cancer. Gynecol Oncol. 2016;143(2):406–13.
37. Meng F, et al. miR-193a-3p regulation of chemoradiation resistance in oesophageal cancer cells via the PSEN1 gene. Gene. 2016;579(2):139–45.

Publisher's Note